Spectrochimica Acta Part B: Atomic Spectroscopy 222 (2024) 107061

Contents lists available at ScienceDirect

Spectrochimica Acta Part B: Atomic Spectroscopy

journal homepage: www.elsevier.com/locate/sab

LIBS plasma diagnostics with SuperCam on Mars: Implications for quantification of elemental abundances

H.T. Manelski [a,*], R.C. Wiens [a], B. Bousquet [b], P.B. Hansen [c], S. Schröder [c], S. Clegg [d], N.D. Martin [d], A.E. Nelson [d], R.K. Martinez [d], A.M. Ollila [d], A. Cousin [e]

[a] Department of Earth, Atmospheric, and Planetary Sciences, Purdue University, West Lafayette, IN, USA
[b] Institut de chimie de la matière condensée de Bordeaux (ICMCB), Univ. Bordeaux, CNRS, Bordeaux INP, Pessac, France
[c] Institut für Optische Sensorsysteme, Deutsches Zentrum für Luft- und Raumfahrt (DLR), Berlin, Germany
[d] Los Alamos National Laboratory, Los Alamos, NM, USA
[e] Institut de Recherche en Astrophysique et Planetologie (IRAP), Université de Toulouse, CNRS, Toulouse, France

ARTICLE INFO

Keywords:
LIBS
Mars
Plasma temperature
Electron density

ABSTRACT

The Perseverance rover landed in Jezero Crater, Mars, in 2021 to explore an ancient delta for signs of past life and collect samples for a future Mars Sample Return Mission. SuperCam, onboard Perseverance, uses Laser Induced Breakdown Spectroscopy (LIBS) to quantify the elements in the rocks/soils encountered along the rover's traverse. LIBS is desirable for planetary science missions because of its effectiveness at a distance and with different target types (rock, soil, etc). However, decreased laser irradiance with distance and changing coupling efficiency in different targets could cause the physical conditions of the plasma plume to vary, with important implications for SuperCam's elemental calibration. This study examines the characteristics of laser-induced plasmas on Mars by estimating apparent temperature via the multiline Boltzmann plot method and electron density using Stark broadening of the H-α line. We find that apparent plasma temperatures do not decrease with distance or vary systematically with target type (rock vs soil). The variability in plasma temperatures seen on Mars is fully represented in the laboratory dataset used for SuperCam's elemental calibration, which suggests that our elemental calibration is likely robust against observed changes in apparent plasma temperature. These results imply that SuperCam can make reliable LIBS observations to at least 8 m. Estimated electron density is 1.4× higher in soils than rock targets, which is likely related to the dependence of the H-α line on topographic relief, a poorly understood mechanism which contributes to the difficulty of quantifying hydrogen abundance in Mars spectra.

1. Introduction

Laser Induced Breakdown Spectroscopy (LIBS) is a versatile technique for rapid and in-situ quantification of major elements in geologic samples [1]. LIBS is appealing for planetary science missions because of its ability to detect essentially all elements (including low-Z elements) [2–6], utility at a range of distances [7,8], and ability to blow away dust [7]. To date, LIBS instruments have flown on three Mars rovers [7,9–12] and one lunar rover [13]. SuperCam is an instrument on the mast of Perseverance Mars rover which employs several techniques, including LIBS, to understand the chemistry and mineralogy of rocks and soils [9,14]. In the LIBS technique, a laser beam is focused and fired at a target, generating a plasma. As the plasma cools and the excited atoms, ions, and molecules in the plasma relax, photons are emitted with an energy characteristic of the various elements and molecules present in the plasma, which are detected by SuperCam. Multivariate methods are then commonly applied to convert a LIBS spectrum into estimated weight percent of major-element oxides [15]. These methods typically use a variety of emission lines of a given element in different parts of the spectrum to make their predictions.

The emission lines observed in LIBS reflect the elemental/molecular composition of the sample but are also strongly affected by the physical conditions in the plasma plume. Plasma temperature and electron density are two parameters often used to describe Laser-Induced Plasmas (LIPs) [1,16]. Plasma temperature affects the balance of neutral vs ionic species. Specifically, at higher temperatures ionic species emit more

* Corresponding author at: Purdue University, Department of Earth, Atmospheric, and Planetary Sciences, 550 Stadium Mall Drive, West Lafayette, IN 47907, USA.
E-mail address: hmanelsk@purdue.edu (H.T. Manelski).

https://doi.org/10.1016/j.sab.2024.107061
Received 22 May 2024; Received in revised form 25 October 2024; Accepted 28 October 2024
Available online 1 November 2024

strongly compared to neutral species [16]. Higher electron density results in wider emission lines, a process known as Stark broadening [16,17]. Temperature and electron density vary throughout the lifetime of LIPs: shortly after initiation the plasmas are hot and dense, rapidly expanding and cooling with time. For a plasma to be adequately described by a single temperature and electron density, it must be in local thermodynamic equilibrium (LTE) [18]. The validity of this assumption in different atmospheric conditions and on different timescales is debated [18,19]. When LTE is present, the proportion of atoms emitting photons at different transitions is described by the Boltzmann distribution. SuperCam LIBS data is obtained time-integrated over several microseconds, and it is clear that LTE is not maintained over this time window and that the derived temperatures should be seen as proxies for typical mean temperatures of martian LIPs. For the purposes of this work, the validity of the apparent plasma temperatures will therefore be mainly assessed by the conformity of observed emission lines to the Boltzmann distribution.

LIPs are inherently short lived. Within tens of ns after the laser pulse hits the target the continuum is emitted [1]. The continuum consists of broad emission resulting from electrons and is not used in our process of elemental abundance quantification. Emission lines from neutral atoms, singly and some doubly ionized atoms, and simple molecules are then observed as atomic and molecular recombination occurs [1].

A number of studies have investigated the behavior of LIPs in laboratory settings with Mars-like atmosphere or the vacuum conditions as on the Moon, however there have been very few studies of plasma diagnostics published using data from in-situ observations on other planetary bodies. For example, plasma temperature and electron density were reported in the lab for a variety of pressures in Knight et al. [20]. An estimate of apparent temperatures was made for plasmas under Mars pressure using the ChemCam instrument before launch [7]. Mars-pressure atmospheric studies have shown that the lifetime of a LIP is strongly dependent on the ambient atmospheric pressure and composition [21]. The thin Martian atmosphere (~610 Pa) means that the expanding LIPs are less confined than on Earth, leading to lower electron densities and thus a shorter time during which LTE conditions apply [21]. Plasma imaging in Mars-like atmospheric conditions has revealed that strong temperature gradients and variations in zones of emission can exist in LIPs [22]. We are aware of only one study [23] that characterized LIP conditions using data from another planetary body; Stetzler et al. presented estimated plasma temperatures based on ChemCam data, but did not explore the source of its variability or the possible effect on elemental calibration [23]. Our work focuses on investigating plasma diagnostics (a temperature proxy and electron density) with SuperCam LIBS on Mars and examining the effect that variability in plasma conditions may have on our elemental calibration.

2. Material and methods

2.1. Apparent plasma temperatures

SuperCam is an instrument on the mast of Perseverance which employs several techniques, including LIBS, to understand the chemistry and mineralogy of rocks and soils encountered by the rover [9,14]. For LIBS, SuperCam uses a diode-pumped Nd:YAG laser which emits light at 1064 nm in 4 ns pulses [9,14]. After the laser pulse hits the target, the emissions of light from the resulting LIP are collected by three spectrometers: ultraviolet (UV), violet (VIO), and the transmission spectrometer, which covers the green, orange, and red ranges [9]. As a result of its requirement to support Raman spectroscopy, the transmission spectrometer (535–853 nm) is also capable of making time-resolved measurements [9,14], while the other two spectrometers, like those of their predecessor, ChemCam [7], are not gated. SuperCam's transmission spectrometer uses an intensifier gate which can be delayed up to milliseconds with a temporal resolution of ~10 ns [9]. For a typical LIBS observation, the intensifier gate is opened as the laser is fired and is closed after 10 microseconds, by which time effectively all the atomic and molecular emissions have been recorded [9]. SuperCam LIBS is commonly used on targets at distances between 2 and 6.5 m, but experiments have been performed up to ~15 m on Mars. A SuperCam LIBS observation typically consists of 30 laser shots at 3 Hz, where the first five shots are used to remove dust cover. SuperCam has taken over 190,000 LIBS spectra on Mars (as of this writing in May 2024) and provided key insights into the igneous crater floor lithologies [24–26] and the nature of volatile-rich alteration phases [27]. In addition to the LIBS data collected on Mars, 2381 spectra were taken using the SuperCam engineering qualification model (EQM) at Los Alamos National Laboratory (LANL) as part of the elemental calibration. These spectra represent 765 targets which are pressed pellets, shot in three locations for 30 shots each from ~3 m away. While Martian targets can be divided into two main groups due to their physical matrix (i.e., rocks and soils), the pressed pellets measured in the laboratory are expected to provide data closer to the rock targets than soils.

To determine apparent temperatures in laser-induced plasmas, multi-line Boltzmann plots were constructed. In this technique, many spectral lines of a given species (e.g. Ca I) are compared and their ratios yield a temperature estimate. The Boltzmann plot method is based on the following equation involving intensity and temperature:

$$ln(I\lambda/gA) = -E_U/kT - ln(4\pi Z/hcN_0) \quad (1)$$

where I is the spectral line radiant intensity, λ is the wavelength of the transition, g is the degeneracy, A is the transition probability, E_U is the upper energy of the electronic transition responsible for the emission line, k is the Boltzmann constant, T is the temperature, Z is the partition function, h is Plank's constant, c is the speed of light, and N_0 is the total species population [28]. Plotting $ln(I\lambda/gA)$ against the upper energy level (E_U) will therefore result in a straight line with a slope of $-1/kT$. At a basic level, the Pearson correlation coefficient (r) of the Boltzmann plot constructed using Eq. (1) can be used as an indication of the validity of the calculated temperature [29]. The slope of the Boltzmann plot should be negative, so temperatures derived from plots with an r close to −1 are more likely to be accurate reflections of plasma conditions. For the spectral line radiant intensity (I) in Eq. (1) to be calculated, the spectrometer must be calibrated in intensity. This was done by observing a Labsphere calibration lamp to determine SuperCam's instrument response function in each spectrometer [30].

Choosing the appropriate spectral lines to include in the Boltzmann plot is not trivial. Well-spaced upper energy levels (E_U) among the lines are desirable, as they result in more precise plasma temperatures. Weak spectral lines should be avoided as they may be more affected by variable signal-to-noise (SNR). Very strong lines should also be avoided because they are the most likely to experience detector saturation or self-absorption, which results in a decrease in the observed spectral intensity [31]. To minimize differences in instrument sensitivity across spectral ranges, lines were chosen within as small a wavelength range as possible. Calcium and iron were selected for use in Boltzmann plots because of their relatively high abundances and number of lines (Table 1). Spectral intensity of each of the LIBS lines was measured using the peak area of a Lorentzian fit modelled in Python (Fig. 1) using the Lmfit package [32]. Any interfering LIBS lines were modelled and removed to isolate the relevant peak.

It should be noted that this study uses neutral (rather than ionic) LIBS lines. Boltzmann plots constructed with neutral lines are known to predict lower apparent temperatures compared to those made with ionic lines [29]. This is because neutral lines are longer lived and therefore reflect a later and cooler phase of the plasma development [1,29]. It is therefore difficult to make meaningful comparisons between apparent plasma temperatures estimated using neutral lines, such as in this study, and ionic lines, including those presented in Wiens et al. [7].

There are numerous complications, both theoretical and practical, in using the Boltzmann method to estimate plasma temperature. For a plasma to be defined by a single temperature, it must be in LTE, optically

Table 1
LIBS lines selected for estimating plasma temperature using Boltzmann plots [33].

Species	λ (nm)*	gA (10^8 s^{-1})	E_U (eV)
Ca I	559.167	0.42	4.73
Ca I	559.602	1.90	4.73
Ca I	560.004	1.30	4.73
Ca I	610.441	0.29	3.91
Ca I	612.391	0.86	3.91
Ca I	616.388	1.43	3.91
Ca I	644.085	4.80	4.45
Ca I	646.436	3.30	4.44
Ca I	649.557	2.20	4.43
Fe I	385.746	0.23	3.26
Fe I	387.967	0.19	3.28
Fe I	388.738	0.37	3.24
Fe I	389.676	0.09	3.29
Fe I	390.081	0.13	3.26
Fe I	392.137	0.08	3.28
Fe I	392.402	0.09	3.21
Fe I	404.695	7.76	4.54
Fe I	406.474	4.66	4.60
Fe I	407.289	3.82	4.65
Fe I	427.296	2.51	4.38
Fe I	430.911	3.04	4.43
Fe I	432.698	3.61	4.47
Fe I	440.599	2.48	4.37

* Vacuum wavelengths are given, as the observations were made at Mars pressure, < 1 kPa, very close to vacuum.

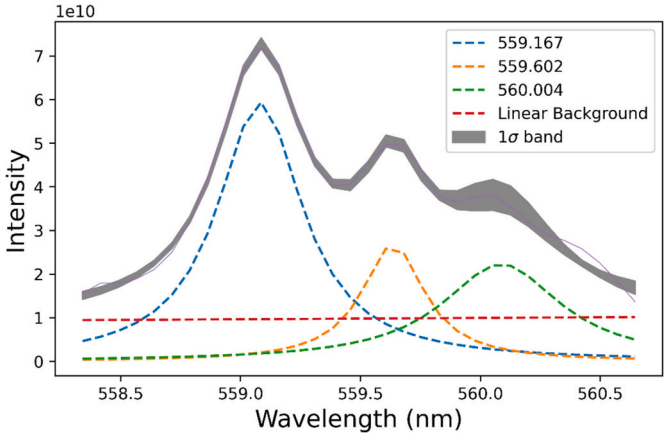

Fig. 1. Example of peak fitting with Lmfit (Python) for three Ca I peaks used for estimation of apparent plasma temperature. This LIBS spectrum was point #1 of the target "Maaz" from Sol 12. In gray are 1σ confidence bands of the peak fits.

thin, and isothermal [18]. This is not expected for SuperCam LIBS observations made in Martian atmospheric conditions with integration times of several microseconds. It has been estimated that, at Earth atmospheric pressure, LIPs generated by an irradiance $>10^8$ W.cm^{-2} would be thermalized enough within several hundred nanoseconds after initiation to ensure LTE, only for small time gates [1]. The irradiance of SuperCam's laser has been calculated to be >10 times greater than this requirement even at 6+ meters [14], but how long LTE would last after initiation during a typical LIBS observation is not known. There is observational evidence that in the thin Mars atmosphere, LTE is a valid assumption for a shorter window of the life of the LIP [21]. The spectra taken at LANL which are used to train multivariate models for elemental calibration [15] and SuperCam spectra on Mars are both time-integrated over a range (10 microseconds after the laser fires in the transmission spectrometer, several milliseconds for the VIO/UV) for which LTE surely not a valid assumption. For this reason, the phrase "apparent plasma temperature" is used in our work.

LIBS spectra with a narrower time-gate are more likely to reflect LTE [34], making their Boltzmann plots a better window into the true physical conditions in the plasma plume. To assess the temporal development of LIPs in an analog Mars atmosphere, a time-resolved experiment was conducted with the SuperCam EQM at LANL. In this experiment, the transmission spectrometer measured the LIBS signal of a gypsum sample with a 100 ns gate width, moving in 50 ns intervals from the initiation of the plasma to 2.4 μs. Plasma temperatures at each interval were calculated using the Ca I lines present in the range of the transmission spectrometer (Table 1).

2.2. Electron density

Apparent electron density in SuperCam LIPs was estimated via Stark broadening of the H-α line (656.45 nm). Stark broadening of the H-α line is well studied because of the strength of the transition and the sensitivity of hydrogen to electric fields generated by free electrons [35]. In this method, the full width at half maximum (FWHM) of the H-α is measured and related to the electron density (N_e) using the following formula (2) which has been theoretically and experimentally determined [17,36]:

$$\mathrm{FWHM} = 1.098\ \mathrm{nm} \times \left(\frac{N_e}{10^{23}\ \mathrm{m}^{-3}}\right)^{0.67965} \quad (2)$$

FWHM was measured by modelling the H-α and the nearby C-II line (Fig. 2) in Python with Lmfit [32].

Spectrometer-induced peak broadening must be considered when measuring Stark broadening. Spectra of a neon lamp taken by SuperCam were used to estimate an instrumental resolution of ~0.4 nm FWHM in the transmission spectrometer. To estimate the FWHM from Stark Broadening, a Voigt was fit to the H-α line where the Gaussian FWHM contribution was set to 0.4 nm (instrument broadening) and the Lorentzian was allowed to vary (Stark broadening). Apparent electron density was estimated using only the Lorentzian FWHM contribution to the Voigt fit.

Doppler broadening is another mechanism which widens spectral lines, but it is negligible (~picometers) compared to Stark broadening in this case [1].

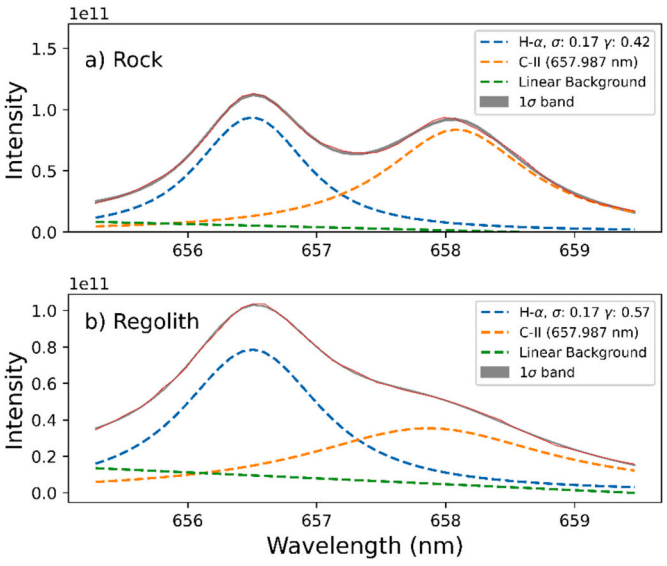

Fig. 2. Example of peak fitting of a rock (a) and regolith target (b) with Lmfit (Python) for the H-α line, used to estimate electron density, and a nearby carbon line. The LIBS spectrum in (a) is point #1 from "Iina" on sol 28 with a H-α FWHM of 1.001 ± 0.019 nm ($N_e = 6.65 \times 10^{22}$ m^{-3}, after accounting for instrument broadening). (b) is point #2 of "As Dzoh" and has a H-α FWHM of 1.301 ± 0.022 nm ($N_e = 1.01 \times 10^{23}$ m^{-3}). In gray are 1σ confidence bands of the peak fits.

Typical 1σ uncertainties FWHM with Lmfit are ~0.02 nm (roughly 2 %), which equates to a roughly 2×10^{21} (~5 %) uncertainty in electron density.

3. Results

3.1. Apparent plasma temperatures

Apparent plasma temperatures and electron density were calculated for 6489 SuperCam LIBS spectra from Mars (up to sol 1066, i.e., the 1066th Martian day of the mission) and 2381 spectra from the calibration database taken in the cleanroom at LANL. For the latter, a Mars-analogue atmosphere of 667 Pa surrounded the samples which consisted pressed powder pellets, and which were located 2.9–3.0 m from the instrument, as this is close to the median distance for the Mars observations.

There is no significant correlation between apparent plasma temperature and distance (Fig. 3, $\rho = -0.12$, where ρ is Spearman's rank correlation coefficient). A correlation coefficient so close to zero indicates that very little of the variability in temperature can be attributed to changes in distance.

The median apparent plasma temperature of SuperCam LIPs on Mars is ~5600 K and ~ 8600 K, using Ca I and Fe I lines respectively (Fig. 4). For Fe I temperatures, only Mars data >3 m were included because of uncertainty with the instrument response in the VIO spectrometer at closer range, a known complication which the SuperCam team is working to better understand.

Fig. 4a shows the distribution of apparent plasma temperatures calculated using Ca I lines in rock (red) and regolith (blue). The two-sample Kolmogorov-Smirnov (KS) test was applied to determine the likelihood that regolith and rock plasma temperatures represent equivalent distributions [38]. The *p*-value of the KS test was 0.0004, indicating that the cumulative distribution functions of regolith and rock Ca I plasma temperatures are significantly different. The median values of the distributions are, however, very similar. The median apparent plasma temperature using Ca I lines for rock is ~5780 K, ~5870 K for regolith (Fig. 4), and ~ 6090 K for lab spectra (Fig. 5).

Note the ~2400 K difference between the median apparent plasma temperatures derived from Fe I vs Ca I lines. This could be due to these species emitting at different times in the evolution of the LIP, although this cannot be evaluated without time-resolved spectra. It is also possible it is an instrument effect, possibly related to the timing of the gate opening and/or integration time of the violet vs transmission spectrometers. For each element studied, spectral lines were chosen to be within a single spectrometer range (VIO for Fe and transmission for Ca) to minimize the impact of potential variability in instrument response between emission lines; the ~2400 K difference in Ca I and Fe I apparent temperatures could indicate there is in fact a meaningful change in instrument response between spectrometers. If this was the case, the apparent temperatures discussed may be not representative of the physical temperature of the plasma plume. Given the interest in understanding the effect of variability in plasma conditions on

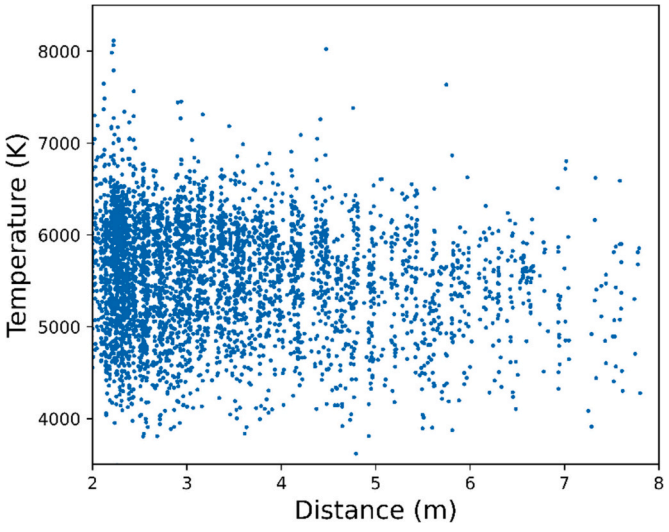

Fig. 3. Apparent plasma temperature of SuperCam LIPs on Mars, estimated based on Ca I, plotted against distance to the target. Only the most well correlated Boltzmann plots ($r < -0.8$) were included (4383 observations).

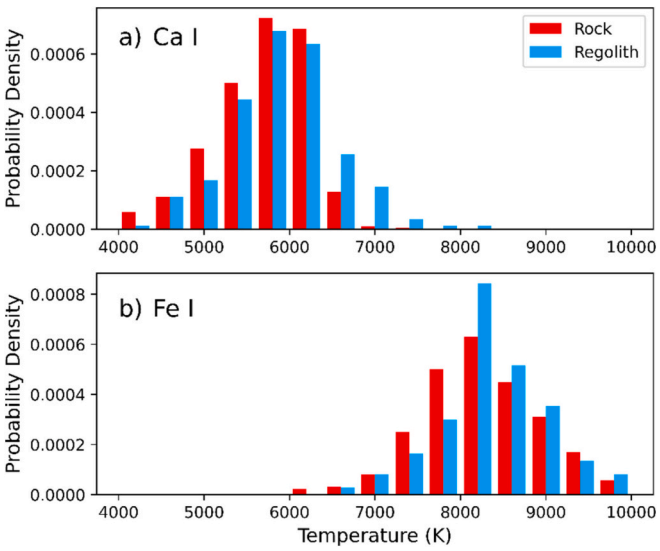

Fig. 4. Histograms of apparent plasma temperature in SuperCam Mars LIBS spectra measured using Ca I (a) and (b) Fe I lines. Only the most well correlated Boltzmann plots ($r < -0.8$) were included (1829 for Ca I and 1182 for Fe I). It is colored by target type (rock in red and regolith in blue). It is a probability density histogram, meaning that each category is normalized to have the same area. Targets on Mars were manually classified as rock vs soil as part of the quarterly PDS release for SuperCam [37]. (For interpretation of the references to colour in this figure legend, the reader is referred to the web version of this article.)

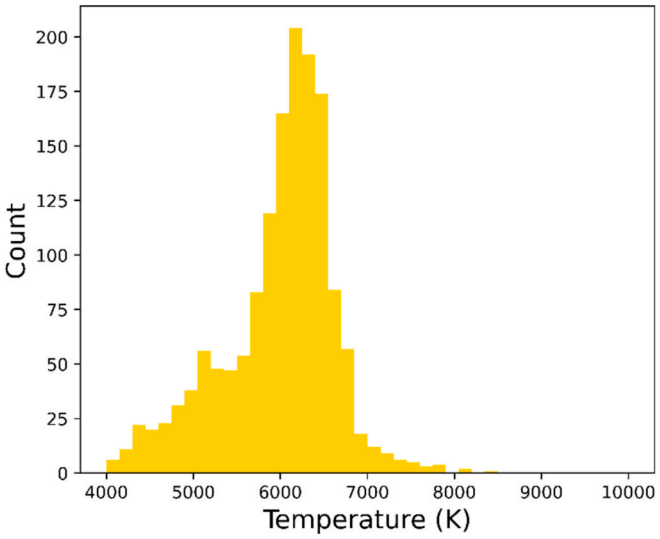

Fig. 5. A histogram of apparent plasma temperature found using Ca I lines for LIBS spectra taken with SuperCam's EQM at LANL in Mars atmospheric conditions for the elemental calibration. Only temperatures derived from a Boltzmann plot with $r < -0.8$ were included (1550 out of the 2381 total lab spectra).

SuperCam's elemental calibration, this possible mismatch in apparent temperature is worth noting but does not impair this work, (as Fe I and Ca I are considered separately).

The median apparent Fe I plasma temperature in different target types is similar (~8230 K for rock and ~ 8340 K for regolith). These values (Fig. 4b) are on the lower edge of the 8670–10,740 K range of LIP excitation temperatures measured in Mars atmospheric conditions with a laboratory setup similar to SuperCam [39]. The range of excitation temperatures reported in Sallé et al. [39] were also derived from spectra which were not sensitively time-gated (the plasma was recorded from 200 to 700 ns after the laser was fired). The ~2000 K distribution in Fe I plasma temperatures is also consistent with the spread reported in the different sample compositions (basalt vs trachyte vs gabbro, etc.) in Sallé et al. [39].

The average apparent plasma temperature from LIBS spectra based on Ca I lines in the LANL calibration dataset is ~6090 K (Fig. 4), which is similar to what is observed for rocks and soils on Mars (Fig. 4a).

Boltzmann plots for Ca I have a median r of −0.88 and Fe I Boltzmann plots have a median r of −0.87 (Fig. S1). The Pearson correlation coefficient (r) of the Boltzmann plots for Ca I are correlated with the weight percent CaO predicted by LIBS (Fig. S2a, $\rho = -0.74$). This suggests that if there is sufficient calcium in the sample (>5 wt%), the Boltzmann plots will generally be very well correlated. A similar trend is visible for Fe I Boltzmann plots (Fig. S2b, $\rho = -0.62$). One limitation of using multiline Boltzmann plots for approximating apparent plasma temperature is the possibility that 'well-correlated' Boltzmann plots are merely the result of chance. The observation that most plots are well correlated overall (Fig. S1) and spectra with stronger Ca I lines are better correlated (Fig. S2) suggests this is unlikely.

To examine the stability of apparent plasma temperatures on homogenous/well-characterized samples, the standard deviation (σ) of each target shot at LANL as part of the elemental calibration was assessed. The median standard deviation of apparent temperatures was 290 K (Ca I lines, Fig. 6a) and 140 K (Fe I lines, Fig. 6b). When looking at the targets with the most well correlated Boltzmann plots ($r < -0.8$), the median standard deviation of apparent temperatures is lower: 210 K for Ca I lines and 94 K for Fe I lines.

3.2. Electron density

The number density of electrons in LIPs on Mars was estimated by measuring the Stark broadening of the H-α line, after accounting for spectrometer-induced instrument broadening. The median electron density is ~0.7×10^{23} m^{-3} for rock targets and ~ 1.1×10^{23} m^{-3} for regolith (Fig. 7). This range of electron densities is consistent with what has been measured for LIPs in laboratory experiments in Mars atmospheric conditions [22] and those predicted by modelling [19].

Millimeter-scale surface roughness has been observed to cause variations in H-α peak area in ChemCam data [40]. This can lead to an overestimation of hydrogen by 1–2 wt% on rough versus flat surfaces [40]. Here, we observe a ~ 30 % difference in median apparent electron density between rocks and soils in SuperCam Mars data (Fig. 7). This corresponds to ~0.3 nm higher FWHM of the H-α in soils than in rock targets (Fig. 7).

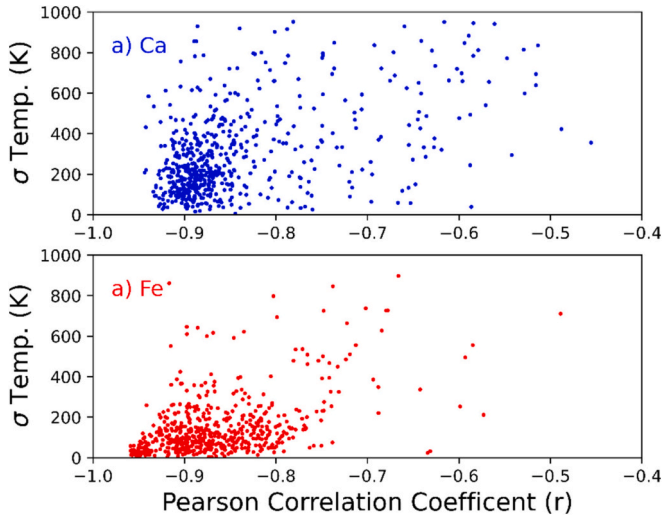

Fig. 6. Standard deviation of apparent plasma temperature derived from Ca I (a) and Fe I lines (b) vs average Boltzmann plot Pearson correlation coefficient (r) for each target shot with the SuperCam EQM at LANL.

3.3. Time-resolved LIBS spectra

A time-resolved LIBS experiment was conducted at LANL using the SuperCam EQM. The transmission spectrometer (535–853 nm) was time-gated with a width of 100 ns, moving over 50 ns in each observation from plasma initiation to 2.4 microseconds. Each observation was averaged over 30 shots to increase SNR. Plasma temperature was estimated using Ca I lines (Table 1), which are all within the range of the transmission spectrometer.

There is a rapid decrease in temperature after the initiation of plasma formation (Fig. 8, blue), with apparent temperature settling around ~6500 K after ~700 ns. This is close to the median apparent temperature predicted for LANL calibration data in time-integrated spectra (Fig. 5). There is a corresponding trend of Boltzmann plot Pearson correlation coefficient (Fig. S3). ~200 ns after the laser fires, the Boltzmann plots appear to be well correlated with an $r < -0.8$. At early times, the Boltzmann plots are very poorly correlated. This is mirrored by a drop in electron density, which also appears to level off at ~0.3×10^{23} m^{-3} at ~700 ns (Fig. 8, red). This is below the average apparent electron density in time-integrated measurements from LANL (Fig. 7). Electron density data after 1600 ns was not included in Fig. 8, as the H-α signal has decayed too much to predict reliable N_e beyond this point (Fig. 9).

Both the H-α and C-II peak decay quickly after reaching maximum intensity ~200 ns. H-α, a neutral line, maintains its intensity for a longer time than C-II. This is consistent with time-resolved experiments that

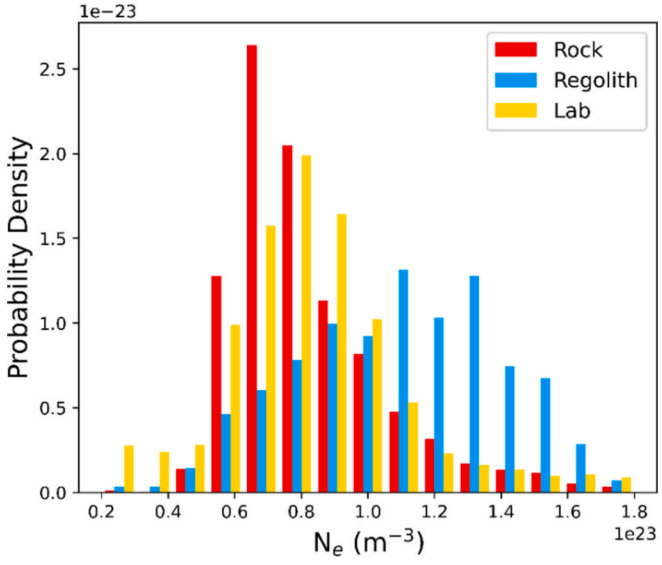

Fig. 7. A histogram of electron density, colored by target type (rock vs regolith) with laboratory spectra taken at LANL shown in gold. It is a probability density histogram, meaning that each category is normalized to have the same area. Targets on Mars were manually classified as rock vs soil as part of the quarterly PDS release for SuperCam [37].

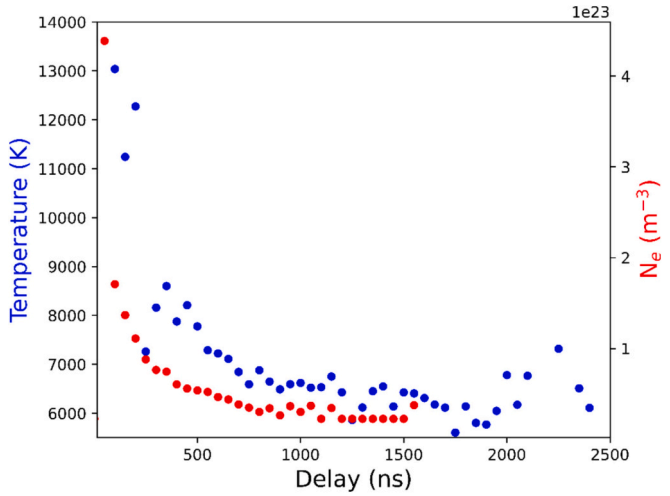

Fig. 8. Temperature (left, blue) and electron density (right, red) vs delay in a time-resolved experiment preformed at LANL with the SuperCam EQM. Electron density data beyond 1.6 microseconds was not included because the hydrogen line is extremely weak at longer time delays and therefore the predicted electron densities are not reliable. (For interpretation of the references to colour in this figure legend, the reader is referred to the web version of this article.)

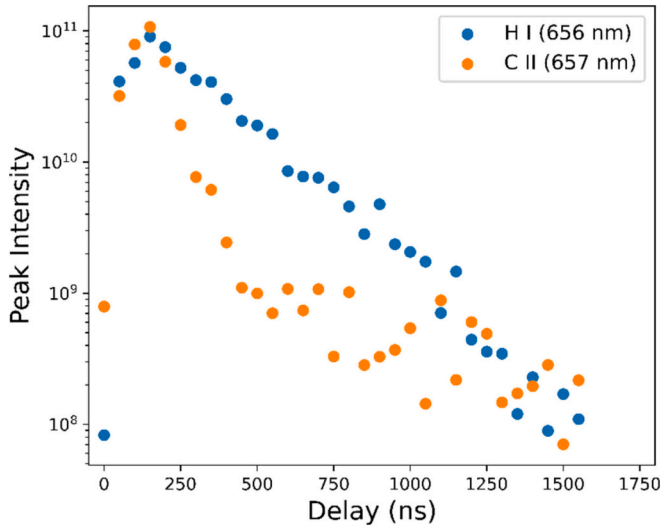

Fig. 9. Peak area plotted against delay in a time-resolved experiment performed at LANL with the SuperCam EQM. Blue is the H-α line (656.467 nm) and orange are two nearby C-II lines (657.987 nm) which are not individually resolved in SuperCam data. (For interpretation of the references to colour in this figure legend, the reader is referred to the web version of this article.)

have been conducted with similar laboratory setups [22].

4. Discussion

LIBS is a powerful technique for elemental analysis of planetary missions because of its reliability at a range of distances (2–6.5 m in the case of SuperCam) and on different types of targets (rocks vs soil) with no sample preparation necessary. However, for SuperCam's multivariate elemental calibration to be effective at various distances and with different target types, assumptions must be made about the physical conditions in the plasma plume. A decrease in effective laser irradiance at longer distances or change in coupling efficiency in loose targets (soil) has the potential to affect the generation and development of the plasma plume, and therefore our elemental calibration. In this section we will discuss the results presented above, especially looking to implications for the applicability and stability of the elemental calibration.

Looking at the best Boltzmann plots ($r < -0.8$) in SuperCam Mars data, the average apparent plasma temperature derived from Ca I lines is 5628 K. The difference in apparent temperature between rock and regolith targets is ~100 K, which is significantly less than the average standard deviation in homogenous targets shot with SuperCam's engineering model at Los Alamos National Laboratory (±210 K). Given that the median standard deviation of apparent Ca I plasma temperatures in well-mixed laboratory standards (Fig. 6) is over twice the median difference between temperatures in rocks and soils in SuperCam Mars data (Fig. 4), it is clear that the observed variability in plasma temperatures is accounted for in our training data. A similar argument can be made for apparent temperatures derived from Fe I lines, although a known complication with the instrument response in the VIO region prevents a direct comparison between Mars and LANL data at the current time. Comparing the most well-correlated Boltzmann plots is important to ensure that the most accurate apparent temperature estimates are juxtaposed, but it does introduce a bias. The most well-correlated Boltzmann plots are derived from spectra with strong Ca I and Fe I lines and therefore relatively high wt% Ca and Fe, respectively (Fig. S2). Spectra without strong Ca I or Fe I lines have poor Boltzmann plots whose derived temperatures are not reliable, and therefore cannot be used to examine trends with distance or target type. SuperCam targets with low Ca (<3 wt%) and low FeO_T (<5 wt%) are rare (140 out of 6489, 2.15 %), but the inability to address this subset of targets is a limitation of this work.

Plasma temperature affects the balance between ionic and neutral species: higher temperature LIPs will have stronger ionized lines. Titanium and iron have many singly ionized lines, so it is plausible that SuperCam's models might underpredict wt% TiO_2 or FeO_T at higher plasma temperatures. This was not observed. No major element predicted by SuperCam was correlated ($\sigma > 0.4$ or $\sigma < -0.4$) with apparent plasma temperatures estimated using Ca I lines in Mars data (Fig. 10). Elements were predicted from SuperCam LIBS spectra using the multivariate algorithms outlined in Anderson et al. 2022 [15].

The ChemCam instrument, the predecessor of SuperCam, on the Curiosity rover, showed systematic trends in elemental abundance with distance in data from Mars [41]. K, Na, Al, and Si all proved sensitive to distance to the target [41]. This was hypothesized to result from lower plasma temperatures with distance. K, Na, Al, and Si have strong emission lines with low upper energy levels, which persist at longer distances (as plasma temperature drops). After the spectrum is normalized this results in proportionally stronger K, Na, Al, and Si lines.

Diffraction of SuperCam's laser at longer distances results in larger ablation craters and lower power densities, which should yield lower plasma temperatures. This would make SuperCam similarly susceptible to geochemical trends with distance. However, no correlation between distance (to 8 m) and apparent plasma temperature or major element predictions was observed in this work (Fig. 10). There are multiple possible reasons why this is the case. SuperCam's aluminum mirror is an improvement over ChemCam's Ni-plated mirror, resulting in sharper focus at longer distances [12,14]. Proof of this is the fact that ChemCam does not ignite a plasma on bedrock beyond ~7 m, while SuperCam has produced plasmas on bedrock at >14 m; the two instruments emit approximately the same energy per pulse, so the difference in capability is due to the focus quality of the beam. Better focus of the laser could result in plasma temperatures decaying more slowly at further distances. SuperCam's elemental abundance predictions are the result of a larger selection of multivariate methods (e.g. OLS, PLS, LASSO, etc.) that may be sensitive to different emission lines than ChemCam's algorithms. In addition, the SuperCam selection of algorithms and parameters was based partly on their performance at various distances (1.55 to 4.25 m) [15], a factor which likely increased SuperCam's resistance to distance effects. By contrast, ChemCam's calibration only used a single distance

	SiO_2	FeO_T	TiO_2	K_2O	MgO	CaO	Al_2O_3	Na_2O	Temp.	r	N_e	Distance
SiO_2	1	-0.29	0.07	0.2	-0.19	-0.25	0.16	0.08	-0.03	0.09	-0.08	0.02
FeO_T	-0.29	1	-0.42	-0.49	0.52	-0.29	-0.57	-0.28	-0.25	0.31	0.15	0.03
TiO_2	0.07	-0.42	1	0.28	-0.62	0.44	0.67	0.4	0.33	-0.37	0.3	0.14
K_2O	0.2	-0.49	0.28	1	-0.47	0	0.47	0.38	0.13	-0.11	-0.18	-0.21
MgO	-0.19	0.52	-0.62	-0.47	1	-0.45	-0.64	-0.46	-0.4	0.36	0.04	0.21
CaO	-0.25	-0.29	0.44	0	-0.45	1	0.35	0.41	0.4	-0.75	0.09	0.07
Al_2O_3	0.16	-0.57	0.67	0.47	-0.64	0.35	1	0.58	0.3	-0.37	-0.02	0.01
Na_2O	0.08	-0.28	0.4	0.38	-0.46	0.41	0.58	1	0.25	-0.41	0.04	0.05
Temp.	-0.03	-0.25	0.33	0.13	-0.4	0.4	0.3	0.25	1	-0.33	0.04	-0.09
r	0.09	0.31	-0.37	-0.11	0.36	-0.75	-0.37	-0.41	-0.33	1	-0.03	-0.02
N_e	-0.08	0.15	0.3	-0.18	0.04	0.09	-0.02	0.04	0.04	-0.03	1	0.35
Distance	0.02	0.03	0.14	-0.21	0.21	0.07	0.01	0.05	-0.09	-0.02	0.35	1

Fig. 10. A Spearman's σ correlation matrix with the major elements predicted by SuperCam in all Mars LIBS spectra (6489 observations), plasma temperature (estimated using Ca I lines), Boltzmann plot Pearson correlation coefficient (r) for Ca I, electron density, and distance. Blue or red indicates a strong positive or negative correlation, respectively. (For interpretation of the references to colour in this figure legend, the reader is referred to the web version of this article.)

[42]. It is also possible that the fine-grained nature of the Murry Formation in Gale Crater enabled the chemical trends with distance to become visible. The mudstones and fine-grained sandstones in Gale are more homogenous on the scale of SuperCam/ChemCam's LIBS ablation size (~200–600 μm) than the igneous materials found in the Jezero Crater floor and the more coarse sandstones of the Jezero delta top [14,43].

The Boltzmann plot Pearson correlation coefficient (r) is highly negatively correlated with the predicted wt% of CaO (Fig. 10. S2). The more calcium in a sample, the stronger the Ca I lines are, which leads to a better correlation coefficient of the Boltzmann plot and a more reliable estimate for apparent plasma temperature. Ca is concentrated in mineral phases (diopside, calcite, etc.), which appears to make Boltzmann plot correlation coefficient moderately correlated with a variety of other major elements (Fig. 10).

SuperCam's LIBS laser beam deposits 75 % of its energy within 170–470 μm for target distances of 2–7 m [14]. The laser pits result from ablation; material in contact with the beam becomes a rapidly expanding plasma, blows away any loose material, and a cavity is formed. Laser pits in rocks are approximately 30 μm deep for 30 laser shots [7,9]. The much deeper LIBS craters in soils (Fig. 11; actual depth not known) are expected to change plasma properties (temperature and electron density), because of enhanced confinement [44–46]. Plasma in a LIBS crater should be hotter and denser [45]. However, as the crater grows deeper, cooling of the plasma as it interacts with the crater walls should eventually result in a decrease in plasma temperature [44]. Given the relationship between target type and LIBS crater depth, systematic variations in apparent temperature and electron density between rocks and soils can be used to probe these expected changes in plasma dynamics. No systematic differences between apparent temperature are observed in rocks vs soils (Fig. 3) in this study; this suggests that the mechanisms of confinement and cooling in craters are either in balance or have very little effect on the Fe I and Ca I emission lines investigated. The effect of self-absorption in soil targets could also affect SuperCam's elemental calibration [46], but self-absorption only has a significant effect on a handful of the strongest LIBS peaks [19] – none of which were examined in this study.

Electron density was estimated from the FWHM of the H-α line and is not affected by the same spectra selection criteria as apparent temperature, making it more likely to reflect the physical state of plasma conditions. Electron density has a different distribution between rock and soil targets on Mars (Fig. 7). The median electron density is ~4.7×10^{22} m^{-3} for rock targets and ~ 7.6×10^{22} m^{-3} for regolith (Fig. 7); this corresponds to a ~ 0.4 nm increase in the FWHM of the H-α line (Fig. 2).

Rapin et al. 2017 reported on a relationship between topographic relief of the target surface and the H-α intensity, highlighting soils as a class of target particularly affected in ChemCam Mars data [40]. Rapin et al. conducted laboratory experiments which demonstrated that mm-scale cavities result in 2–4 times the H-α/Ca I line peak area ratio as a flat surface [40].

In Fig. 12 we see evidence of this topographic effect in SuperCam Mars data. Regolith targets have a much higher H-α peak area relative to nearby Ca I lines, compared to rock targets. While this could be explained by adsorbed water in soils, Rapin et al. showed that geometry alone could recreate this affect with ChemCam in a simulated Martian atmosphere [40].

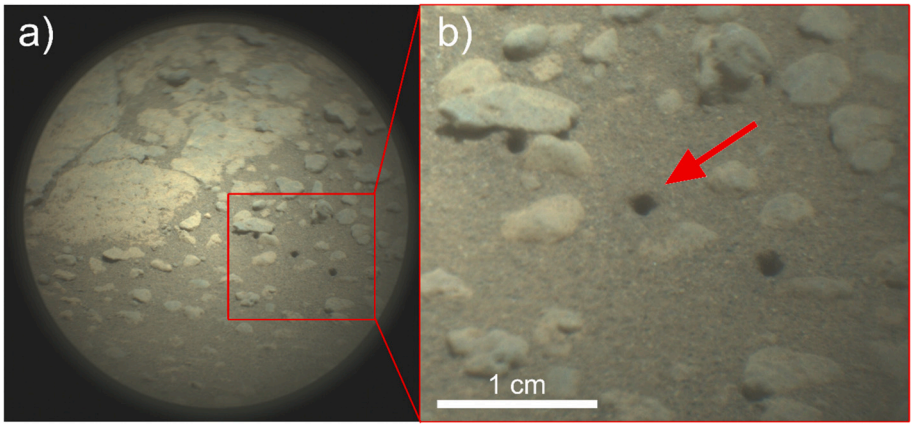

Fig. 11. A SuperCam Remote Micro Imager (RMI) image of the "As Dzoh" regolith target from Sol 103. a) is the full RMI image and b) is a cropped image with a red arrow pointing to the pits created by LIBS in soil. (For interpretation of the references to colour in this figure legend, the reader is referred to the web version of this article.)

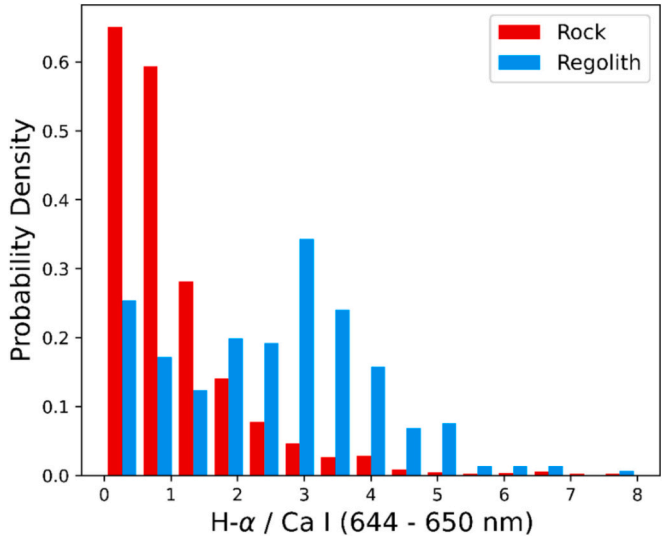

Fig. 12. A histogram of the ratio of H-α peak area against the sum of nearby Ca I lines (644.085 nm, 646.436 nm, and 649.557 nm) for SuperCam Mars data. Blue is regolith/soil targets and rock targets are in red. It is a probability density histogram, meaning that each category is normalized to have the same area.

It is possible that the variability in apparent electron density in SuperCam Mars data presented in this work can be explained by two mechanisms: (1) ion-induced desorption [40], which increases the intensity of the H-α emission and (2) subsequent self-absorption broadening. This would explain both the apparent difference in FWHM of the H-α line and the similarity in plasma temperatures between rocks and soils, but it is unclear the extent to which the H-α line is susceptible to self-absorption broadening. Confinement alone would explain the increased electron density in soils but would not account for the observations in Rapin et al. or the lack of a change in apparent plasma temperature in rocks vs soils. Martian soils, especially at finer-grain sizes, can have a composition quite different from the surrounding rock [47], which could also account for some variability in plasma properties. Soils often have a stronger hydrated component, but this alone would result in a higher amplitude H-α line and not a significant change in the FWHM.

The laboratory spectra presented in Section 3.3 provide plasma temperatures and electron densities over a narrow time-gate (100 ns) and provide further information on the physical conditions in the plasma plume. As expected, the plume is hot and dense at the earliest times (Fig. 8). Between 0.5 and 1 microseconds the plasma appears to plateau at ~6500 K and $N_e = \sim 0.3 \times 10^{23}$ m^{-3}. Fig. 9 demonstrates that there is a significant difference in the emission timing of the H-α compared to the interfering C-II line, suggesting that these lines would be more easily separated at longer time-delays (500+ ns). Therefore, given that Mars' atmosphere is dominated by CO_2, longer time-delays may be desirable for detecting hydrogen with SuperCam on Mars.

We are confident, based on this time-resolved experiment, that while LTE is not a reasonable assumption for typical time-integrated SuperCam, the apparent temperatures and electron densities presented in this work reflect an 'average' which captures both the unstable initial dynamics (<0.5 μs) and stable plasma conditions in later times (>0.5 μs).

5. Conclusions

In this work, we investigate the conditions of laser-induced plasmas on Mars with SuperCam for the first time, using apparent temperature and electron density. The decrease in laser irradiance with distance was suspected to result in a drop in apparent plasma temperature, with important implications for our elemental calibration, but this was not observed within the distances of 2–8 m. The vast majority of spectra used to train SuperCam's major element algorithms were taken at LANL at ~3 m, but the distribution of plasma temperatures in these laboratory spectra are nearly identical to the spread of temperatures seen on Mars (2–6.5 m). While it is true that apparent plasma temperature might be expected to decrease with distance, these results indicate this effect is minimal on the range of typical SuperCam targets. SuperCam's LIBS distance limit therefore may result from rapidly deteriorating focus >8 m and eventually an inability to generate a spark, rather than a steady decrease in plasma temperature. This increases the SuperCam team's confidence in the elemental calibration at longer distances and also helps explain the lack of elemental/distance trends in SuperCam Mars data, in contrast to those seen with ChemCam [41]. The variability in apparent temperatures between different types of targets (rock vs soil) and chemistries is also well represented in the LANL dataset used to train algorithms for our elemental calibration. This suggests that the multivariate algorithms used to quantify the major elements are robust against the variability in apparent plasma temperature observed on Mars and strengthens confidence in SuperCam data at longer distances.

The electron density of LIPs generated on Martian soils was ~1.4× that of rock targets. This corresponds to a ~ 0.3 nm difference in the FWHM of the H-α line. There is no correlation between electron density and any of the major elements predicted by SuperCam. It is likely that this is related to the connection between the intensity of the hydrogen signal and topographic relief, as explored in Rapin et al. [40]. It could be caused by a combination of ion-induced desorption and self-absorption, but spatiotemporally resolved LIBS experiments in simulated Martian atmosphere are required to test this hypothesis.

Finally, we present time-resolved LIBS experiments with SuperCam's EQM, which indicate that although LTE is not a valid assumption for our usual time-integrated spectra on Mars, apparent plasma temperatures/electron densities are an average which reflects the unstable initial plasma dynamics and later plasma conditions.

CRediT authorship contribution statement

H.T. Manelski: Writing – review & editing, Writing – original draft, Visualization, Validation, Software, Resources, Project administration, Methodology, Investigation, Formal analysis, Data curation, Conceptualization. **R.C. Wiens:** Writing – review & editing, Validation, Supervision, Resources, Project administration, Investigation, Funding acquisition, Data curation, Conceptualization. **B. Bousquet:** Writing – review & editing, Validation, Methodology, Investigation, Formal analysis. **P.B. Hansen:** Writing – review & editing, Methodology, Investigation. **S. Schröder:** Writing – review & editing, Methodology. **S. Clegg:** Resources, Data curation. **N.D. Martin:** Investigation. **A.E. Nelson:** Resources, Data curation. **R.K. Martinez:** Data curation. **A.M. Ollila:** Resources, Conceptualization. **A. Cousin:** Resources.

Declaration of competing interest

We have no known conflicts of interest to report.

Data availability

Data will be made available on request.

Acknowledgements

This project was supported in the United States by the NASA Mars Exploration Program and LANL and in France by CNES and CNRS. Support in Germany was provided by DLR.

Appendix A. Supplementary data

Supplementary data to this article can be found online at https://doi.org/10.1016/j.sab.2024.107061.

References

[1] D.A. Cremers, L.J. Radziemski, Handbook of Laser-Induced Breakdown Spectroscopy, 1st ed, Wiley, 2013, https://doi.org/10.1002/9781118567371.

[2] W. Rapin, P.-Y. Meslin, S. Maurice, R.C. Wiens, D. Laporte, B. Chauviré, O. Gasnault, S. Schröder, P. Beck, S. Bender, O. Beyssac, A. Cousin, E. Dehouck, C. Drouet, O. Forni, M. Nachon, N. Melikechi, B. Rondeau, N. Mangold, N. H. Thomas, Quantification of water content by laser induced breakdown spectroscopy on Mars, Spectrochim. Acta B At. Spectrosc. 130 (2017) 82–100, https://doi.org/10.1016/j.sab.2017.02.007.

[3] P.J. Gasda, E.B. Haldeman, R.C. Wiens, W. Rapin, T.F. Bristow, J.C. Bridges, S. P. Schwenzer, B. Clark, K. Herkenhoff, J. Frydenvang, N.L. Lanza, S. Maurice, S. Clegg, D.M. Delapp, V.L. Sanford, M.R. Bodine, R. McInroy, In situ detection of boron by ChemCam on Mars, Geophys. Res. Lett. 44 (2017) 8739–8748, https://doi.org/10.1002/2017GL074480.

[4] A.M. Ollila, H.E. Newsom, B. Clark, R.C. Wiens, A. Cousin, J.G. Blank, N. Mangold, V. Sautter, S. Maurice, S.M. Clegg, O. Gasnault, O. Forni, R. Tokar, E. Lewin, M. D. Dyar, J. Lasue, R. Anderson, S.M. McLennan, J. Bridges, D. Vaniman, N. Lanza, C. Fabre, N. Melikechi, G.M. Perrett, J.L. Campbell, P.L. King, B. Barraclough, D. Delapp, S. Johnstone, P. Meslin, A. Rosen-Gooding, J. Williams, The MSL science team, trace element geochemistry (Li, Ba, Sr, and Rb) using *Curiosity* 's ChemCam: early results for Gale crater from Bradbury landing site to Rocknest, JGR Planets 119 (2014) 255–285, https://doi.org/10.1002/2013JE004517.

[5] P. Beck, P.Y. Meslin, A. Fau, O. Forni, O. Gasnault, J. Lasue, A. Cousin, S. Schröder, S. Maurice, W. Rapin, R.C. Wiens, A.M. Ollila, E. Dehouck, N. Mangold, B. Garcia, S. Schwartz, W. Goetz, N. Lanza, Detectability of carbon with ChemCam LIBS: distinguishing sample from Mars atmospheric carbon, and application to Gale crater, Icarus 408 (2024) 115840, https://doi.org/10.1016/j.icarus.2023.115840.

[6] O. Forni, M. Gaft, M.J. Toplis, S.M. Clegg, S. Maurice, R.C. Wiens, N. Mangold, O. Gasnault, V. Sautter, S. Le Mouélic, P. Meslin, M. Nachon, R.E. McInroy, A. M. Ollila, A. Cousin, J.C. Bridges, N.L. Lanza, M.D. Dyar, First detection of fluorine on Mars: implications for Gale Crater's geochemistry, Geophys. Res. Lett. 42 (2015) 1020–1028, https://doi.org/10.1002/2014GL062742.

[7] R.C. Wiens, S. Maurice, B. Barraclough, M. Saccoccio, W.C. Barkley, J.F. Bell, S. Bender, J. Bernardin, D. Blaney, J. Blank, M. Bouyé, N. Bridges, N. Bultman, P. Caïs, R.C. Clanton, B. Clark, S. Clegg, A. Cousin, D. Cremers, A. Cros, L. DeFlores, D. Delapp, R. Dingler, C. D'Uston, M. Darby Dyar, T. Elliott, D. Enemark, C. Fabre, M. Flores, O. Forni, O. Gasnault, T. Hale, C. Hays, K. Herkenhoff, E. Kan, L. Kirkland, D. Kouach, D. Landis, Y. Langevin, N. Lanza, F. LaRocca, J. Lasue, J. Latino, D. Limonadi, C. Lindensmith, C. Little, N. Mangold, G. Manhes, P. Mauchien, C. McKay, E. Miller, J. Mooney, R.V. Morris, L. Morrison, T. Nelson, H. Newsom, A. Ollila, M. Ott, L. Pares, R. Perez, F. Poitrasson, C. Provost, J. W. Reiter, T. Roberts, F. Romero, V. Sautter, S. Salazar, J.J. Simmonds, R. Stiglich, S. Storms, N. Striebig, J.-J. Thocaven, T. Trujillo, M. Ulibarri, D. Vaniman, N. Warner, R. Waterbury, R. Whitaker, J. Witt, B. Wong-Swanson, The ChemCam Instrument Suite on the Mars Science Laboratory (MSL) Rover: body unit and combined system tests, Space Sci. Rev. 170 (2012) 167–227, https://doi.org/10.1007/s11214-012-9902-4.

[8] K.Y. Kane, D.A. Cremers, Remote elemental analysis of planetary surfaces using laser-induced breakdown, Spectroscopy 23 (1992) 651.

[9] R.C. Wiens, S. Maurice, S.H. Robinson, A.E. Nelson, P. Cais, P. Bernardi, R. T. Newell, S. Clegg, S.K. Sharma, S. Storms, J. Deming, D. Beckman, A.M. Ollila, O. Gasnault, R.B. Anderson, Y. André, S. Michael Angel, G. Arana, E. Auden, P. Beck, J. Becker, K. Benzerara, S. Bernard, O. Beyssac, L. Borges, B. Bousquet, K. Boyd, M. Caffrey, J. Carlson, K. Castro, J. Celis, B. Chide, K. Clark, E. Cloutis, E. C. Cordoba, A. Cousin, M. Dale, L. Deflores, D. Delapp, M. Deleuze, M. Dirmyer, C. Donny, G. Dromart, M. George Duran, M. Egan, J. Ervin, C. Fabre, A. Fau, W. Fischer, O. Forni, T. Fouchet, R. Fresquez, J. Frydenvang, D. Gasway, I. Gontijo, J. Grotzinger, X. Jacob, S. Jacquinod, J.R. Johnson, R.A. Klisiewicz, J. Lake, N. Lanza, J. Laserna, J. Lasue, S. Le Mouélic, C. Legett, R. Leveille, E. Lewin, G. Lopez-Reyes, R. Lorenz, E. Lorigny, S.P. Love, B. Lucero, J.M. Madariaga, M. Madsen, S. Madsen, N. Mangold, J.A. Manrique, J.P. Martinez, J. Martinez-Frias, K.P. McCabe, T.H. McConnochie, J.M. McGlown, S.M. McLennan, N. Melikechi, P.-Y. Meslin, J.M. Michel, D. Mimoun, A. Misra, G. Montagnac, F. Montmessin, V. Mousset, N. Murdoch, H. Newsom, L.A. Ott, Z.R. Ousnamer, L. Pares, Y. Parot, R. Pawluczyk, C. Glen Peterson, P. Pilleri, P. Pinet, G. Pont, F. Poulet, C. Provost, B. Quertier, H. Quinn, W. Rapin, J.-M. Reess, A.H. Regan, A. L. Reyes-Newell, P.J. Romano, C. Royer, F. Rull, B. Sandoval, J.H. Sarrao, V. Sautter, M.J. Schoppers, S. Schröder, D. Seitz, T. Shepherd, P. Sobron, B. Dubois, V. Sridhar, M.J. Toplis, I. Torre-Fdez, I.A. Trettel, M. Underwood, A. Valdez, J. Valdez, D. Venhaus, P. Willis, The SuperCam Instrument Suite on the NASA Mars 2020 Rover: body unit and combined system tests, Space Sci. Rev. 217 (2021) 4, https://doi.org/10.1007/s11214-020-00777-5.

[10] W. Xu, X. Liu, Z. Yan, L. Li, Z. Zhang, Y. Kuang, H. Jiang, H. Yu, F. Yang, C. Liu, T. Wang, C. Li, Y. Jin, J. Shen, B. Wang, W. Wan, J. Chen, S. Ni, Y. Ruan, R. Xu, C. Zhang, Z. Yuan, X. Wan, Y. Yang, Z. Li, Y. Shen, D. Liu, B. Wang, R. Yuan, T. Bao, R. Shu, The MarSCoDe instrument Suite on the Mars rover of China's Tianwen-1 Mission, Space Sci. Rev. 217 (2021) 64, https://doi.org/10.1007/s11214-021-00836-5.

[11] X. Wan, Design, Function, and Implementation of China's First LIBS Instrument (MarSCoDe) on the Zhurong Mars Rover, At.Spectrosc. 42 (2021), https://doi.org/10.46770/AS.2021.608.

[12] S. Maurice, R.C. Wiens, M. Saccoccio, B. Barraclough, O. Gasnault, O. Forni, N. Mangold, D. Baratoux, S. Bender, G. Berger, J. Bernardin, M. Berthé, N. Bridges, D. Blaney, M. Bouyé, P. Caïs, B. Clark, S. Clegg, A. Cousin, D. Cremers, A. Cros, L. DeFlores, C. Derycke, B. Dingler, G. Dromart, B. Dubois, M. Dupieux, E. Durand, L. d'Uston, C. Fabre, B. Faure, A. Gaboriaud, T. Gharsa, K. Herkenhoff, E. Kan, L. Kirkland, D. Kouach, J.-L. Lacour, Y. Langevin, J. Lasue, S. Le Mouélic, M. Lescure, E. Lewin, D. Limonadi, G. Manhès, P. Mauchien, C. McKay, P.-Y. Meslin, Y. Michel, E. Miller, H.E. Newsom, G. Orttner, A. Paillet, L. Parès, Y. Parot, R. Pérez, P. Pinet, F. Poitrasson, B. Quertier, B. Sallé, C. Sotin, V. Sautter, H. Séran, J.J. Simmonds, J.-B. Sirven, R. Stiglich, N. Striebig, J.-J. Thocaven, M. J. Toplis, D. Vaniman, The ChemCam instrument Suite on the Mars science laboratory (MSL) rover: science objectives and mast unit description, Space Sci. Rev. 170 (2012) 95–166, https://doi.org/10.1007/s11214-012-9912-2.

[13] A.S. Laxmiprasad, R.V.L.N. Sridhar, A. Goswami, K.A. Lohar, M.V.H. Rao, K. V. Shila, M. Mahajan, B. Raha, T.S. Smaran, B. Krishnamprasad, Laser induced breakdown spectroscope on Chandrayaan-2 Rover: a miniaturized mid-UV to visible active spectrometer for Lunar surface chemistry studies, Curr. Sci. 118 (2020) 573, https://doi.org/10.18520/cs/v118/i4/573-581.

[14] S. Maurice, R.C. Wiens, P. Bernardi, P. Caïs, S. Robinson, T. Nelson, O. Gasnault, J.-M. Reess, M. Deleuze, F. Rull, J.-A. Manrique, S. Abbaki, R.B. Anderson, Y. André, S.M. Angel, G. Arana, T. Battault, P. Beck, K. Benzerara, S. Bernard, J.-P. Berthias, O. Beyssac, M. Bonafous, B. Bousquet, M. Boutillier, A. Cadu, K. Castro, F. Chapron, B. Chide, K. Clark, E. Clavé, S. Clegg, E. Cloutis, C. Collin, E.C. Cordoba, A. Cousin, J.-C. Dameury, W. D'Anna, Y. Daydou, A. Debus, L. Deflores, E. Dehouck, D. Delapp, G. De Los Santos, C. Donny, A. Doressoundiram, G. Dromart, B. Dubois, A. Dufour, M. Dupieux, M. Egan, J. Ervin, C. Fabre, A. Fau, W. Fischer, O. Forni, T. Fouchet, J. Frydenvang, S. Gauffre, M. Gauthier, V. Gharakanian, O. Gilard, I. Gontijo, R. Gonzalez, D. Granena, J. Grotzinger, R. Hassen-Khodja, M. Heim, Y. Hello, G. Hervet, O. Humeau, X. Jacob, S. Jacquinod, J.R. Johnson, D. Kouach, G. Lacombe, N. Lanza, L. Lapauw, J. Laserna, J. Lasue, L. Le Deit, S. Le Mouélic, E. Le Comte, Q.-M. Lee, C. Legett, R. Leveille, E. Lewin, C. Leyrat, G. Lopez-Reyes, R. Lorenz, B. Lucero, J.M. Madariaga, S. Madsen, M. Madsen, N. Mangold, F. Manni, J.-F. Mariscal, J. Martinez-Frias, K. Mathieu, R. Mathon, K.P. McCabe, T. McConnochie, S.M. McLennan, J. Mekki, N. Melikechi, P.-Y. Meslin, Y. Micheau, Y. Michel, J.M. Michel, D. Mimoun, A. Misra, G. Montagnac, C. Montaron, F. Montmessin, J. Moros, V. Mousset, Y. Morizet, N. Murdoch, R.T. Newell, H. Newsom, N. Nguyen Tuong, A.M. Ollila, G. Orttner, L. Oudda, L. Pares, J. Parisot, Y. Parot, R. Pérez, D. Pheav, L. Picot, P. Pilleri, C. Pilorget, P. Pinet, G. Pont, F. Poulet, C. Quantin-Nataf, B. Quertier, D. Rambaud, W. Rapin, P. Romano, L. Roucayrol, C. Royer, M. Ruellan, B.F. Sandoval, V. Sautter, M. J. Schoppers, S. Schröder, H.-C. Seran, S.K. Sharma, P. Sobron, M. Sodki, A. Sournac, V. Sridhar, D. Standarovsky, S. Storms, N. Striebig, M. Tatat, M. Toplis, I. Torre-Fdez, N. Toulemont, C. Velasco, M. Veneranda, D. Venhaus, C. Virmontois, M. Viso, P. Willis, K.W. Wong, The SuperCam Instrument Suite on the Mars 2020 Rover: science objectives and mast-unit description, Space Sci. Rev. 217 (2021) 47, https://doi.org/10.1007/s11214-021-00807-w.

[15] R.B. Anderson, O. Forni, A. Cousin, R.C. Wiens, S.M. Clegg, J. Frydenvang, T.S. J. Gabriel, A. Ollila, S. Schröder, O. Beyssac, E. Gibbons, D.S. Vogt, E. Clavé, J.-A. Manrique, C. Legett, P. Pilleri, R.T. Newell, J. Sarrao, S. Maurice, G. Arana, K. Benzerara, P. Bernardi, S. Bernard, B. Bousquet, A.J. Brown, C. Alvarez-Llamas, B. Chide, E. Cloutis, J. Comellas, S. Connell, E. Dehouck, D.M. Delapp, A. Essunfeld, C. Fabre, T. Fouchet, C. Garcia-Florentino, L. García-Gómez, P. Gasda, O. Gasnault, E.M. Hausrath, N.L. Lanza, J. Laserna, J. Lasue, G. Lopez, J.M. Madariaga, L. Mandon, N. Mangold, P.-Y. Meslin, A.E. Nelson, H. Newsom, A.L. Reyes-Newell, S. Robinson, F. Rull, S. Sharma, J.I. Simon, P. Sobron, I.T. Fernandez, A. Udry, D. Venhaus, S.M. McLennan, R.V. Morris, B. Ehlmann, Post-landing major element quantification using SuperCam laser induced breakdown spectroscopy, Spectrochim. Acta B At. Spectrosc. 188 (2022) 106347, https://doi.org/10.1016/j.sab.2021.106347.

[16] R. Noll, Laser-Induced Breakdown Spectroscopy: Fundamentals and Applications, 2012th ed., Springer Berlin Heidelberg Springer e-books, Berlin, Heidelberg, 2012.

[17] M. Burger, J. Hermann, Stark broadening measurements in plasmas produced by laser ablation of hydrogen containing compounds, Spectrochim. Acta B At. Spectrosc. 122 (2016) 118–126, https://doi.org/10.1016/j.sab.2016.06.005.

[18] G. Cristoforetti, A. De Giacomo, M. Dell'Aglio, S. Legnaioli, E. Tognoni, V. Palleschi, N. Omenetto, Local thermodynamic equilibrium in laser-induced breakdown spectroscopy: beyond the McWhirter criterion, Spectrochim. Acta B At. Spectrosc. 65 (2010) 86–95, https://doi.org/10.1016/j.sab.2009.11.005.

[19] P.B. Hansen, S. Schröder, S. Kubitza, K. Rammelkamp, D.S. Vogt, H.-W. Hübers, Modeling of time-resolved LIBS spectra obtained in Martian atmospheric conditions with a stationary plasma approach, Spectrochim. Acta B At. Spectrosc. 178 (2021) 106115, https://doi.org/10.1016/j.sab.2021.106115.

[20] A.K. Knight, N.L. Scherbarth, D.A. Cremers, M.J. Ferris, Characterization of laser-induced breakdown spectroscopy (LIBS) for application to space exploration, Appl. Spectrosc. 54 (2000) 331–340, https://doi.org/10.1366/0003702001949591.

[21] F. Colao, R. Fantoni, V. Lazic, A. Paolini, LIBS application for analyses of martian crust analogues: search for the optimal experimental parameters in air and CO 2 atmosphere, Appl. Phys. A Mater. Sci. Process. 79 (2004) 143–152, https://doi.org/10.1007/s00339-003-2262-x.

[22] D.S. Vogt, S. Schröder, S. Frohmann, P.B. Hansen, F. Seel, M. Gensch, H.-W. Hübers, Spatiotemporal characterization of the laser-induced plasma plume in simulated Martian conditions, Spectrochim. Acta B At. Spectrosc. 187 (2022) 106326, https://doi.org/10.1016/j.sab.2021.106326.

[23] J. Stetzler, S. Tang, R.C. Chinni, Plasma temperature and Electron density determination using laser-induced breakdown spectroscopy (LIBS) in Earth's and Mars's atmospheres, Atoms 8 (2020) 50, https://doi.org/10.3390/atoms8030050.

[24] R.C. Wiens, A. Udry, O. Beyssac, C. Quantin-Nataf, N. Mangold, A. Cousin, L. Mandon, T. Bosak, O. Forni, S.M. McLennan, V. Sautter, A. Brown, K. Benzerara, J.R. Johnson, L. Mayhew, S. Maurice, R.B. Anderson, S.M. Clegg, L. Crumpler, T.S. J. Gabriel, P. Gasda, J. Hall, B.H.N. Horgan, L. Kah, C. Legett, J.M. Madariaga, P.-

Y. Meslin, A.M. Ollila, F. Poulet, C. Royer, S.K. Sharma, S. Siljeström, J.I. Simon, T. E. Acosta-Maeda, C. Alvarez-Llamas, S.M. Angel, G. Arana, P. Beck, S. Bernard, T. Bertrand, B. Bousquet, K. Castro, B. Chide, E. Clavé, E. Cloutis, S. Connell, E. Dehouck, G. Dromart, W. Fischer, T. Fouchet, R. Francis, J. Frydenvang, O. Gasnault, E. Gibbons, S. Gupta, E.M. Hausrath, X. Jacob, H. Kalucha, E. Kelly, E. Knutsen, N. Lanza, J. Laserna, J. Lasue, S. Le Mouélic, R. Leveille, G. Lopez Reyes, R. Lorenz, J.A. Manrique, J. Martinez-Frias, T. McConnochie, N. Melikechi, D. Mimoun, F. Montmessin, J. Moros, N. Murdoch, P. Pilleri, C. Pilorget, P. Pinet, W. Rapin, F. Rull, S. Schröder, D.L. Shuster, R.J. Smith, A.E. Stott, J. Tarnas, N. Turenne, M. Veneranda, D.S. Vogt, B.P. Weiss, P. Willis, K.M. Stack, K. H. Williford, K.A. Farley, The SuperCam Team, Compositionally and density stratified igneous terrain in Jezero crater, Mars, Sci. Adv. 8 (2022), https://doi.org/10.1126/sciadv.abo3399 eabo3399.

[25] A. Udry, A. Ostwald, V. Sautter, A. Cousin, O. Beyssac, O. Forni, G. Dromart, K. Benzerara, M. Nachon, B. Horgan, L. Mandon, E. Clavé, E. Dehouck, E. Gibbons, S. Alwmark, E. Ravanis, R.C. Wiens, C. Legett, R. Anderson, P. Pilleri, N. Mangold, M. Schmidt, Y. Liu, J.I. Núñez, K. Castro, J.M. Madariaga, T. Kizovski, P. Beck, S. Bernard, T. Bosak, A. Brown, S. Clegg, E. Cloutis, B. Cohen, S. Connell, L. Crumpler, V. Debaille, D. Flannery, T. Fouchet, T.S.J. Gabriel, O. Gasnault, C.D. K. Herd, J. Johnson, J.A. Manrique, S. Maurice, F.M. McCubbin, S. McLennan, A. Ollila, P. Pinet, C. Quantin-Nataf, C. Royer, S. Sharma, J.I. Simon, A. Steele, N. Tosca, A. Treiman, the SuperCam team, A Mars 2020 Perseverance SuperCam perspective on the igneous nature of the Máaz formation at Jezero crater and link with Séítah, Mars, JGR Planets 128 (2023), https://doi.org/10.1029/2022JE007440 e2022JE007440.

[26] O. Beyssac, O. Forni, A. Cousin, A. Udry, L.C. Kah, L. Mandon, O.E. Clavé, Y. Liu, F. Poulet, C. Quantin Nataf, O. Gasnault, J.R. Johnson, K. Benzerara, P. Beck, E. Dehouck, N. Mangold, C. Alvarez Llamas, R.B. Anderson, G. Arana, R. Barnes, S. Bernard, T. Bosak, A.J. Brown, K. Castro, B. Chide, S.M. Clegg, E. Cloutis, T. Fouchet, T. Gabriel, S. Gupta, G. Lacombe, J. Lasue, S. Le Mouelic, G. Lopez-Reyes, J.M. Madariaga, F.M. McCubbin, S.M. McLennan, J.A. Manrique, P. Y. Meslin, F. Montmessin, J. Núñez, A.M. Ollila, A. Ostwald, P. Pilleri, P. Pinet, C. Royer, S.K. Sharma, S. Schröder, J.I. Simon, M.J. Toplis, M. Veneranda, P. A. Willis, S. Maurice, R.C. Wiens, The SuperCam Team, Petrological Traverse of the Olivine Cumulate Séítah Formation at Jezero Crater, Mars: a perspective from SuperCam onboard perseverance, JGR Planets 128 (2023), https://doi.org/10.1029/2022JE007638 e2022JE007638.

[27] E. Clavé, K. Benzerara, P.-Y. Meslin, O. Forni, C. Royer, L. Mandon, P. Beck, C. Quantin-Nataf, O. Beyssac, A. Cousin, B. Bousquet, R.C. Wiens, S. Maurice, E. Dehouck, S. Schröder, O. Gasnault, N. Mangold, G. Dromart, T. Bosak, S. Bernard, A. Udry, R.B. Anderson, G. Arana, A.J. Brown, K. Castro, S.M. Clegg, E. Cloutis, A.G. Fairén, D.T. Flannery, P.J. Gasda, J.R. Johnson, J. Lasue, G. Lopez-Reyes, J.M. Madariaga, J.A. Manrique, S. Le Mouélic, J.I. Núñez, A.M. Ollila, P. Pilleri, C. Pilorget, P. Pinet, F. Poulet, M. Veneranda, Z.U. Wolf, the SuperCam team, Carbonate Detection With SuperCam in Igneous Rocks on the Floor of Jezero Crater, Mars, JGR Planets 128 (2023), https://doi.org/10.1029/2022JE007463 e2022JE007463.

[28] B. Bousquet, V. Gardette, V.M. Ros, R. Gaudiuso, M. Dell'Aglio, A. De Giacomo, Plasma excitation temperature obtained with Boltzmann plot method: significance, precision, trueness and accuracy, Spectrochim. Acta B At. Spectrosc. 204 (2023) 106686, https://doi.org/10.1016/j.sab.2023.106686.

[29] J.A. Aguilera, C. Aragón, Characterization of a laser-induced plasma by spatially resolved spectroscopy of neutral atom and ion emissions, Spectrochim. Acta B At. Spectrosc. 59 (2004) 1861–1876, https://doi.org/10.1016/j.sab.2004.08.003.

[30] C. Legett, R.T. Newell, A.L. Reyes-Newell, A.E. Nelson, P. Bernardi, S.C. Bender, O. Forni, D.M. Venhaus, S.M. Clegg, A.M. Ollila, P. Pilleri, V. Sridhar, S. Maurice, R.C. Wiens, Optical calibration of the SuperCam instrument body unit spectrometers, Appl. Opt. 61 (2022) 2967, https://doi.org/10.1364/AO.447680.

[31] F. Rezaei, G. Cristoforetti, E. Tognoni, S. Legnaioli, V. Palleschi, A. Safi, A review of the current analytical approaches for evaluating, compensating and exploiting self-absorption in Laser Induced Breakdown Spectroscopy, Spectrochim. Acta B At. Spectrosc. 169 (2020) 105878, https://doi.org/10.1016/j.sab.2020.105878.

[32] M. Newville, T. Stensitzki, D.B. Allen, A. Ingargiola, LMFIT: Non-Linear Least-Square Minimization and Curve-Fitting for Python, 2014, https://doi.org/10.5281/ZENODO.11813.

[33] A. Kramida, Y. Ralchenko, NIST Atomic Spectra Database, NIST Standard Reference Database 78, 1999, https://doi.org/10.18434/T4W30F.

[34] G. Cristoforetti, E. Tognoni, L.A. Gizzi, Thermodynamic equilibrium states in laser-induced plasmas: from the general case to laser-induced breakdown spectroscopy plasmas, Spectrochim. Acta B At. Spectrosc. 90 (2013) 1–22, https://doi.org/10.1016/j.sab.2013.09.004.

[35] L. Yang, X. Tan, X. Wan, L. Chen, D. Jin, M. Qian, G. Li, Stark broadening for diagnostics of the electron density in non-equilibrium plasma utilizing isotope hydrogen alpha lines, J. Appl. Phys. 115 (2014) 163106, https://doi.org/10.1063/1.4873960.

[36] M.A. Gigosos, M.Á. González, V. Cardeñoso, Computer simulated Balmer-alpha, −beta and -gamma Stark line profiles for non-equilibrium plasmas diagnostics, Spectrochim. Acta B At. Spectrosc. 58 (2003) 1489–1504, https://doi.org/10.1016/S0584-8547(03)00097-1.

[37] Sylvestre A. Maurice, Roger C. Wiens, Mars 2020 SuperCam Bundle, (n.d.). doi:10.17189/1522646.

[38] J.W. Pratt, J.D. Gibbons, Kolmogorov-Smirnov Two-Sample Tests, in: Concepts of Nonparametric Theory, Springer, New York, New York, NY, 1981, pp. 318–344, https://doi.org/10.1007/978-1-4612-5931-2_7.

[39] B. Sallé, J.-L. Lacour, P. Mauchien, P. Fichet, S. Maurice, G. Manhès, Comparative study of different methodologies for quantitative rock analysis by Laser-Induced Breakdown Spectroscopy in a simulated Martian atmosphere, Spectrochim. Acta B At. Spectrosc. 61 (2006) 301–313, https://doi.org/10.1016/j.sab.2006.02.003.

[40] W. Rapin, B. Bousquet, J. Lasue, P.-Y. Meslin, J.-L. Lacour, C. Fabre, R.C. Wiens, J. Frydenvang, E. Dehouck, S. Maurice, O. Gasnault, O. Forni, A. Cousin, Roughness effects on the hydrogen signal in laser-induced breakdown spectroscopy, Spectrochim. Acta B At. Spectrosc. 137 (2017) 13–22, https://doi.org/10.1016/j.sab.2017.09.003.

[41] R.C. Wiens, A.J. Blazon-Brown, N. Melikechi, J. Frydenvang, E. Dehouck, S. M. Clegg, D. Delapp, R.B. Anderson, A. Cousin, S. Maurice, Improving ChemCam LIBS long-distance elemental compositions using empirical abundance trends, Spectrochim. Acta B At. Spectrosc. 182 (2021) 106247, https://doi.org/10.1016/j.sab.2021.106247.

[42] S.M. Clegg, R.C. Wiens, R. Anderson, O. Forni, J. Frydenvang, J. Lasue, A. Cousin, V. Payré, T. Boucher, M.D. Dyar, S.M. McLennan, R.V. Morris, T.G. Graff, S. A. Mertzman, B.L. Ehlmann, I. Belgacem, H. Newsom, B.C. Clark, N. Melikechi, A. Mezzacappa, R.E. McInroy, R. Martinez, P. Gasda, O. Gasnault, S. Maurice, Recalibration of the Mars Science Laboratory ChemCam instrument with an expanded geochemical database, Spectrochim. Acta B At. Spectrosc. 129 (2017) 64–85, https://doi.org/10.1016/j.sab.2016.12.003.

[43] F. Rivera-Hernández, D.Y. Sumner, N. Mangold, S.G. Banham, K.S. Edgett, C. M. Fedo, S. Gupta, S. Gwizd, E. Heydari, S. Maurice, M. Nachon, H. Newsom, J. Schieber, K. Stack-Morgan, N. Stein, R.C. Wiens, Grain size variations in the Murray formation: stratigraphic evidence for changing depositional environments in Gale crater, Mars, JGR Planets 125 (2020), https://doi.org/10.1029/2019JE006230 e2019JE006230.

[44] B. Chide, S. Maurice, N. Murdoch, J. Lasue, B. Bousquet, X. Jacob, A. Cousin, O. Forni, O. Gasnault, P.-Y. Meslin, J.-F. Fronton, M. Bassas-Portús, A. Cadu, A. Sournac, D. Mimoun, R.C. Wiens, Listening to laser sparks: a link between laser-induced breakdown spectroscopy, acoustic measurements and crater morphology, Spectrochim. Acta B At. Spectrosc. 153 (2019) 50–60, https://doi.org/10.1016/j.sab.2019.01.008.

[45] M. Corsi, G. Cristoforetti, M. Hidalgo, D. Iriarte, S. Legnaioli, V. Palleschi, A. Salvetti, E. Tognoni, Effect of laser-induced crater depth in laser-induced breakdown spectroscopy emission features, Appl. Spectrosc. 59 (2005) 853–860, https://doi.org/10.1366/0003702054411607.

[46] N.D. Martin, H.T. Manelski, R.C. Wiens, S. Clegg, P.B. Hansen, S. Schröder, B. Chide, LIBS peak broadening in soils on mars, in: Lunar and Planetary Institute, The Woodlands, Texas/Virtual, 2024.

[47] P.-Y. Meslin, O. Gasnault, O. Forni, S. Schröder, A. Cousin, G. Berger, S.M. Clegg, J. Lasue, S. Maurice, V. Sautter, S. Le Mouélic, R.C. Wiens, C. Fabre, W. Goetz, D. Bish, N. Mangold, B. Ehlmann, N. Lanza, A.-M. Harri, R. Anderson, E. Rampe, T. H. McConnochie, P. Pinet, D. Blaney, R. Léveillé, D. Archer, B. Barraclough, S. Bender, D. Blake, J.G. Blank, N. Bridges, B.C. Clark, L. DeFlores, D. Delapp, G. Dromart, M.D. Dyar, M. Fisk, B. Gondet, J. Grotzinger, K. Herkenhoff, J. Johnson, J.-L. Lacour, Y. Langevin, L. Leshin, E. Lewin, M.B. Madsen, N. Melikechi, A. Mezzacappa, M.A. Mischna, J.E. Moores, H. Newsom, A. Ollila, R. Perez, N. Renno, J.-B. Sirven, R. Tokar, M. De La Torre, L. d'Uston, D. Vaniman, A. Yingst, M.S.L. Science Team, O. Kemppinen, M. Minitti, D. Cremers, J.F. Bell, L. Edgar, J. Farmer, A. Godber, M. Wadhwa, D. Wellington, I. McEwan, C. Newman, M. Richardson, A. Charpentier, L. Peret, P. King, G. Weigle, M. Schmidt, S. Li, R. Milliken, K. Robertson, V. Sun, M. Baker, C. Edwards, K. Farley, J. Griffes, H. Miller, M. Newcombe, C. Pilorget, M. Rice, K. Siebach, K. Stack, E. Stolper, C. Brunet, V. Hipkin, G. Marchand, P.S. Sánchez, L. Favot, G. Cody, A. Steele, L. Flückiger, D. Lees, A. Nefian, M. Martin, M. Gailhanou, F. Westall, G. Israël, C. Agard, J. Baroukh, C. Donny, A. Gaboriaud, P. Guillemot, V. Lafaille, E. Lorigny, A. Paillet, R. Pérez, M. Saccoccio, C. Yana, C. Armiens-Aparicio, J.C. Rodríguez, I.C. Blázquez, F.G. Gómez, J. Gómez-Elvira, S. Hettrich, A.L. Malvitte, M.M. Jiménez, J. Martínez-Frías, J. Martín-Soler, F.J. Martín-Torres, A.M. Jurado, L. Mora-Sotomayor, G.M. Caro, S.N. López, V. Peinado-González, J. Pla-García, J.A.R. Manfredi, J.J. Romeral-Planelló, S.A.S. Fuentes, E.S. Martinez, J.T. Redondo, R. Urqui-O'Callaghan, M.-P.Z. Mier, S. Chipera, P. Mauchien, H. Manning, A. Fairén, A. Hayes, J. Joseph, S. Squyres, R. Sullivan, P. Thomas, A. Dupont, A. Lundberg, J. DeMarines, D. Grinspoon, G. Reitz, B. Prats, E. Atlaskin, M. Genzer, H. Haukka, H. Kahanpää, J. Kauhanen, O. Kemppinen, M. Paton, J. Polkko, W. Schmidt, T. Siili, J. Wray, M.B. Wilhelm, F. Poitrasson, K. Patel, S. Gorevan, S. Indyk, G. Paulsen, S. Gupta, J. Schieber, C. Geffroy, D. Baratoux, A. Cros, Q.-M. Lee, E. Pallier, Y. Parot, M. Toplis, W. Brunner, E. Heydari, C. Achilles, D. Oehler, B. Sutter, M. Cabane, D. Coscia, G. Israël, C. Szopa, F. Robert, M. Nachon, A. Buch, F. Stalport, P. Coll, P. François, F. Raulin, S. Teinturier, J. Cameron, R. Dingler, R.S. Jackson, S. Johnstone, C. Little, T. Nelson, R.B. Williams, A. Jones, L. Kirkland, A. Treiman, B. Baker, B. Cantor, M. Caplinger, S. Davis, B. Duston, K. Edgett, D. Fay, C. Hardgrove, D. Harker, P. Herrera, E. Jensen, M.R. Kennedy, G. Krezoski, D. Krysak, L. Lipkaman, M. Malin, E. McCartney, S. McNair, B. Nixon, L. Posiolova, M. Ravine, A. Salamon, L. Saper, K. Stoiber, K. Supulver, J. Van Beek, T. Van Beek, R. Zimdar, K.L. French, K. Iagnemma, K. Miller, R. Summons, F. Goesmann, S. Hviid, M. Johnson, M. Lefavor, E. Lyness, E. Breves, C. Fassett, T. Bristow, D. DesMarais, L. Edwards, R. Haberle, T. Hoehler, J. Hollingsworth, M. Kahre, L. Keely, C. McKay, M. B. Wilhelm, L. Bleacher, W. Brinckerhoff, D. Choi, P. Conrad, J.P. Dworkin, J. Eigenbrode, M. Floyd, C. Freissinet, J. Garvin, D. Glavin, D. Harpold, A. Jones, P. Mahaffy, D.K. Martin, A. McAdam, A. Pavlov, E. Raaen, M.D. Smith, J. Stern, F. Tan, M. Trainer, M. Meyer, A. Posner, M. Voytek, R.C. Anderson, A. Aubrey, L. W. Beegle, A. Behar, D. Brinza, F. Calef, L. Christensen, J.A. Crisp, J. Feldman, S. Feldman, G. Flesch, J. Hurowitz, I. Jun, D. Keymeulen, J. Maki, J.M. Morookian, T. Parker, B. Pavri, M. Schoppers, A. Sengstacken, J.J. Simmonds, N. Spanovich, A. R. Vasavada, C.R. Webster, A. Yen, F. Cucinotta, J.H. Jones, D. Ming, R.V. Morris,

P. Niles, T. Nolan, L. Radziemski, D. Berman, E.N. Dobrea, R.M.E. Williams, K. Lewis, T. Cleghorn, W. Huntress, G. Manhès, J. Hudgins, T. Olson, N. Stewart, P. Sarrazin, J. Grant, E. Vicenzi, S.A. Wilson, M. Bullock, B. Ehresmann, V. Hamilton, D. Hassler, J. Peterson, S. Rafkin, C. Zeitlin, F. Fedosov, D. Golovin, N. Karpushkina, A. Kozyrev, M. Litvak, A. Malakhov, I. Mitrofanov, M. Mokrousov, S. Nikiforov, V. Prokhorov, A. Sanin, V. Tretyakov, A. Varenikov, A. Vostrukhin, R. Kuzmin, M. Wolff, S. McLennan, O. Botta, D. Drake, K. Bean, M. Lemmon, S. P. Schwenzer, E.M. Lee, R. Sucharski, M.Á.D.P. Hernández, J.J.B. Ávalos, M. Ramos, M.-H. Kim, C. Malespin, I. Plante, J.-P. Muller, R. Navarro-González, R. Ewing, W. Boynton, R. Downs, M. Fitzgibbon, K. Harshman, S. Morrison, W. Dietrich, O. Kortmann, M. Palucis, D.Y. Sumner, A. Williams, G. Lugmair, M. A. Wilson, D. Rubin, B. Jakosky, T. Balic-Zunic, J. Frydenvang, J.K. Jensen, K. Kinch, A. Koefoed, S.L.S. Stipp, N. Boyd, J.L. Campbell, R. Gellert, G. Perrett, I. Pradler, S. VanBommel, S. Jacob, T. Owen, S. Rowland, E. Atlaskin, H. Savijärvi, E. Boehm, S. Böttcher, S. Burmeister, J. Guo, J. Köhler, C.M. García, R. Mueller-Mellin, R. Wimmer-Schweingruber, J.C. Bridges, M. Benna, H. Franz, H. Bower, A. Brunner, H. Blau, T. Boucher, M. Carmosino, S. Atreya, H. Elliott, D. Halleaux, N. Rennó, M. Wong, R. Pepin, B. Elliott, J. Spray, L. Thompson, S. Gordon, J. Williams, P. Vasconcelos, J. Bentz, K. Nealson, R. Popa, L.C. Kah, J. Moersch, C. Tate, M. Day, G. Kocurek, B. Hallet, R. Sletten, R. Francis, E. McCullough, E. Cloutis, I.L. Ten Kate, R. Kuzmin, R. Arvidson, A. Fraeman, D. Scholes, S. Slavney, T. Stein, J. Ward, J. Berger, Soil diversity and hydration as observed by ChemCam at Gale Crater, Mars, Science 341 (2013) 1238670, https://doi.org/10.1126/science.1238670.